ADVANCED BIOSYSTEMS
www.adv-biosys.com

Printing Life-Inspired Subcellular Scale Compartments with Autonomous Molecularly Crowded Confinement

Giuseppe Arrabito, Felicia Cavaleri, Alessandro Porchetta, Francesco Ricci, Valeria Vetri, Maurizio Leone, and Bruno Pignataro**

A simple, rapid, and highly controlled platform to prepare life-inspired subcellular scale compartments by inkjet printing has been developed. These compartments consist of fL-scale aqueous droplets (few µm in diameter) incorporating biologically relevant molecular entities with programmed composition and concentration. These droplets are ink-jetted in nL mineral oil drop arrays allowing for lab-on-chip studies by fluorescence microscopy and fluorescence life time imaging. Once formed, fL-droplets are stable for several hours, thus giving the possibility of readily analyze molecular reactions and their kinetics and to verify molecular behavior and intermolecular interactions. Here, this platform is exploited to unravel the behavior of different molecular probes and biomolecular systems (DNA hairpins, enzymatic cascades, protein-ligand couples) within the compartments. The fL-scale size induces the formation of molecularly crowded confined shell structures (hundreds of nanometers in thickness) at the droplet surface, allowing discovery of specific features (e.g., heterogeneity, responsivity to molecular triggers) that are mediated by the intermolecular interactions in these peculiar environments. The presented results indicate the possibility of using this platform for designing nature-inspired confined reactors allowing for a deepened understanding of molecular confinement effects in living subcellular compartments.

1. Introduction

Engineered aqueous compartments with life-like features have stimulated a great interest in the recent years since their application as artificial cells and organelles.[1] The interest for these systems mainly derives from their development as medicine transport systems.[2] Also, artificial and hybrid cells may constitute functional systems to be incorporated in living cells as artificial organelles modulating their functions and processes.[3] For example, artificial organelles with light-harvesting capabilities allow for a sustainable adenosine triphosphate (ATP) energy source,[4] for removing antibiotic in surface waters,[5] and for directing intravesicular reactions.[6] On this respect, it is crucial to recapitulate life-like activities in cellular-mimicking environments such as those compartments enclosing selected sets of biomolecular machineries.[6,7]

As a fundamental feature, eukaryotic living cells, which typically enclose pL-scale volumes (about 10 µm in diameter), localize biochemical machineries into smaller compartments driven by liquid/liquid separation or in membrane-defined organelles. In particular, the more complex activities (transcription, energy production, m-RNA processing, etc.) are orchestrated inside heterogeneous fL-scale compartments (nuclei, mitochondria, P-bodies, etc.) that control the spatiotemporal assembly of biochemical processes under highly regulated conditions.[8] Their diameter is in the range 0.3–5 µm, depending on the enclosing biomolecular systems and their specific features (concentration, degree of molecular self-assembly, solubility, presence of a membrane).[8] On the other hand, more simple activities like transport, signaling, and storage are carried out by even smaller compartments, as the synaptic vesicles, which may reach nanoscopic diameters with volumes in the aL-scale and nanometer size.[9]

The above different size regimes from the pL to the aL scale are expected to present distinct physicochemical features also in connection to their different surface/volume ratios. Focusing on the subcellular systems with more complex activities, different biomacromolecules (DNA, proteins, enzymes) are highly crowded occupying a large part of the compartment volume.[10] Crowding may induce volume exclusion, i.e., limited accessible space and available water molecules for biomolecules.[10] Moreover, crowding is often associated to confinement effects, as evolution has selected the spatial localization of fundamental processes by spontaneous phase separation processes.[11] On this respect, examples include DNA transcription process in bacterial cells[12] or DNA packing in eukaryotic nuclear environments,[13] or mRNA processing enzymes in P-bodies.[14]

Dr. G. Arrabito, Dr. F. Cavaleri, Prof. V. Vetri, Prof. M. Leone, Prof. B. Pignataro
Department of Physics and Chemistry
University of Palermo
Viale delle Scienze, Parco d'Orleans II, 90128 Palermo, Italy
E-mail: valeria.vetri@unipa.it; bruno.pignataro@unipa.it
Dr. A. Porchetta, Prof. F. Ricci
Department of Chemical Science and Technologies
University of Rome
Tor Vergata, Via della Ricerca Scientifica, 00133 Rome, Italy
The ORCID identification number(s) for the author(s) of this article can be found under https://doi.org/10.1002/adbi.201900023.

DOI: 10.1002/adbi.201900023

Crowding and confinement have not been reproduced synergically in micrometric fL-scale subcellular artificial compartments and the correlation between their peculiar surface/volume ratio and the resulting molecular spatial organization and activity needs to be understood. Recent studies show crowding effects in larger pL-scale droplets (about 25 μm in diameter) giving heterogeneous gene expression environments.[15] On the other hand, molecular confinement has been already observed to increase the reaction rate and stereo selectivity of self-assembling nanoflasks,[16] the ribozyme cleavage rate in aqueous compartments,[17] and the spontaneous remodeling of actin networks in ring-shaped bundles.[18]

For these reasons, it is urgent to provide a strategy to combine crowding and confinement of biomolecular systems in artificial subcellular like fL-scale compartments. Different approaches can produce compartments at this scale.[19–24] Direct water-in-oil emulsification permits to obtain water droplets dispersed in oil typically varying in a wide range size (from micro- to nanoscale).[19] Also, DNA nanotechnology provides assembled structures mimicking cellular modules, but it suffers complexity and high costs.[20] Microfluidics approaches enable the preparation of monodisperse fL-scale droplets under high shear stresses, ultimately modifying the distribution of the surfactants needed to stabilize the oil–water interface. In turn, this can lead to the nonspecific adsorption of biomolecules at the oil–water interface which can potentially affect the biological activity.[21] Several reports have shown the possibility to produce fL-droplets following printing approaches as different as pin-printing,[22] ultrafine nozzles printing,[23] hydrodynamic droplet dispensing under electrical field guiding,[24] droplets production within liquid environments,[25] satellite droplets printing,[26] liquid meniscus breakup in a double-orifice system,[27] or spontaneous interfacial droplet fragmentation.[28] However, these printing methods suffer from complex experimental set-ups and require specialized hardware, making difficult their rapid implementation in chemistry laboratories. In comparison to the microfluidics approaches, the printing processes have the advantage to produce droplets on demand with kHz frequencies which can be patterned on solid surfaces allowing for the fabrication of lab-on-chip devices.[29] Also similar to microfluidics, the printing processes are associated with high shear stresses and high pressure strikes which may result in mechanical stresses to the biomolecules.[30]

This paper reports on the realization of a novel platform allowing for the direct printing of life-inspired artificial compartments with well-defined composition and concentration as well as tight dimensional distribution within size scales from the nL to the fL allowing showing the transition effects in the molecular and intermolecular features of incorporated molecular and biomolecular systems. In particular, these compartments are injected in mineral oil drops arrayed on glass substrates by a novel inkjet printing methodology, whereas the molecular structures and activity of the incorporated systems are investigated by advanced fluorescence microscopy and fluorescence life time imaging (FLIM). Interestingly, just in the few μm regime, novel features emerge by autonomous molecularly crowded confinement effects.

2. Results and Discussion

2.1. Printing Highly Controlled Subcellular Scale Aqueous Compartments

Nanoliter- and picoliter-scale homogenous aqueous droplets can be successfully injected in mineral oil drops by inkjet printing aqueous inks on glass surfaces.[31] Here, a novel piezoelectric "spike waveform" (i.e., the voltage vs time signal given to the piezoelectric actuator) is designed (**Figure 1**a) to meet the singularity of the Navier–Stokes equation in the Eggers's theoretical model which predicts the reduction of droplet size by minimizing the droplet formation time.[32] Accordingly, the droplet downscaling up to 15–40 fL (3–4 μm in diameter) from the inkjet printer pL-scale microchannels is possible by minimizing the ejection time (Figure 1b). Note that in spite of the absolute standard deviation values in Figure 1b, the coefficient of variation (standard-deviation/mean ratio) of the fL-droplet radii is higher (about 27% at 0.5 μs) than that of the pL-droplets (12–18% at 1–10 μs), whereas for the liquid threads, it results almost similar in the two different size regimes (10–18%). This is likely due to the larger dimension of the liquid threads than the droplet radii resulting in a smaller experimental uncertainty in the determination of their sizes from the stroboscopic images.

As to the droplet diameter, by following the Eggers's theoretical model, it is possible to downscale its value below the nozzle size (about 10 μm in diameter), if the ejection time is kept at values down to 1 μs. To this purpose, a novel three-phase waveform signal minimizing the jetting time has been designed. Importantly, also the jetting voltage has to be kept as low as possible (between 12 and 14 V) to pull the liquid tongue into the nozzle by forming only fL-droplets (Figure 1c). On the other hand, at high voltages (>15 V), the liquid tongue coalesces with the fL-droplet (Figure 1d) and the droplet regains the standard size of the nozzle. Details on the methodology are reported in Figures S1 and S2 in the Supporting Information.

The fL-sized aqueous droplets are printed in mineral oil drops (see sections 2.2–2.5). In agreement with the water droplet size observed in the mineral oil drops (see section 2.2), the evaporation of the fL-scale water droplets would not significantly occur during their formation. Indeed, by considering its speed (about 4 m s^{-1}) and the distance between the nozzle and the oil drop surface (<1 mm), a typical fL-scale water droplet forms at the nozzle in about 15–20 μs and needs not more than 0.2–0.3 ms to reach the oil drop, whereas by following the model of van der Heijden et al.,[33] the evaporation of 15–40 fL aqueous droplets is predicted in a range of 4–10 ms.

Once engulfed in the mineral oil, the molecules dissolved in these small fL-scale droplets would diffuse in the mineral oil drop. In order to avoid molecular leakage into the oil phase, the fL-droplets are spiked under optimized conditions with a mixture of nonionic surfactants including the di-block copolymer poly(ethylene glycol)-block-poly(propylene glycol)-block-poly(ethylene glycol) (PEG-PPG-PEG) (F108; 0.03% w/v), an efficient amphiphilic stabilizer of oil/water interfaces in emulsion droplets,[34] and Tween-20 (0.05% v/v), already reported as inhibitor of colloidal aggregation in solution.[31]

Along with the stabilization of water/oil interface, the surfactants can modify the ink viscosity and the surface tension,

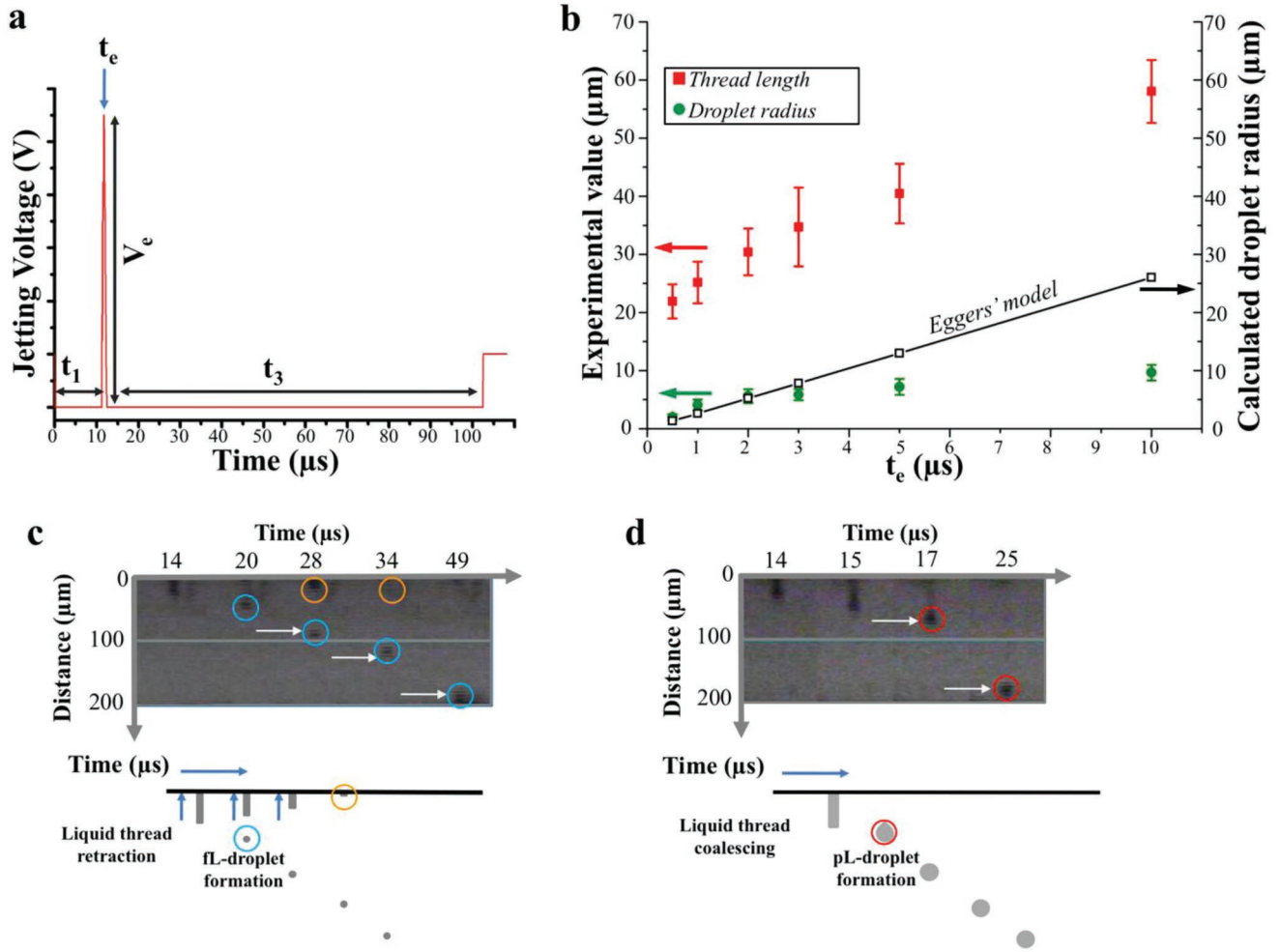

Figure 1. Aqueous femtoliter droplets by minimized inkjet printing ejection time. a) Piezoelectric driving "spike" waveform for ejecting fL-droplets. The ejection phase is equal to 0.5 µs. The pulling phase lasts 90 µs (t_e the time of droplet ejection, t_1 and t_2 the time intervals for liquid pulling back into the nozzle, V_e the jetting potential at droplet ejection). The intervals t_1 and t_3 permit to pull back the liquid tongue in the nozzle orifice. b) Experimental values of the droplet radius at pinch-off (green circle) and thread length (red squares) along with the Egger's model predicting the minimal droplet radius values (hollow squares) plotted as a function of t_e. Each experimental value is the average of five different droplets ($n = 5$), error bars represent standard deviation. c,d) Stroboscopic images of the droplet (water solution of 4×10^{-6} M Atto655-labeled Biotin, 0.03% F108, and 0.05% Tween-20) pinching-off at the nozzles respectively for $12 \le V_e \le 14$ and $15 \le V_e \le 40$. The schemes below show the droplet formation process at the fL-scale and at the conventional pL-scale, respectively. For the fL-scale, a pinch-off occurs after about 20 µs (cyan circle), whereas the liquid tail remains attached at the nozzle and is pulled back after 34 µs (orange circle), allowing reducing the droplet volume below the nozzle size. The pL-scale droplet formation results by the liquid thread coalescing into a single nozzle-sized droplet.

which are both fundamental parameters to ensure fluid printability in inkjet printing.[35] In particular, F108 can slightly increase the ink viscosity already in the 1–4 w/v% range,[36] whereas the Tween-20 effect is in comparison significantly lower.[37] In this regard, it was possible (Figure S3, Supporting Information) to produce fL-droplets at F108 concentrations as high as 3% w/v, corresponding to the typical viscosity limit for inkjet printing of about 20–30 mPa s.[35] On the other hand, it was not possible to produce fL-scale droplets at higher F108 concentrations, the resulting viscosity falling outside from the printable regimes of the Derby plot[35] (see Figure S1 in the Supporting Information), a convenient representation of the fluid properties (viscosity, surface tension, droplet size, and speed) for inkjet printing. As a result, the surfactants at the chosen concentrations (F108 0.03% w/v, Tween-20 0.05% v/v) maintain the droplet viscosity to values similar to unmodified aqueous solutions (1–2 mPa s[36,37]), which are compatible with inkjet printing.

In contrast to viscosity, the ink surface tension decreases with the surfactants amount and it can be estimated of about 35 mN m^{-1}[38,39] at the above concentration values. A decreased surface tension would favor the formation of satellites along with a decreased droplet speed,[40] but in this respect our "spike waveform" pulled the liquid tongue back into the nozzle avoiding the formation of satellites. Thanks to the minimization of the jetting voltage and the jetting time, this waveform is also expected to reduce the mechanical stresses (shear and compression) during the droplet formation process[30,41] allowing the biomolecules to maintain their structure and the functionality (see sections 2.4–2.5).

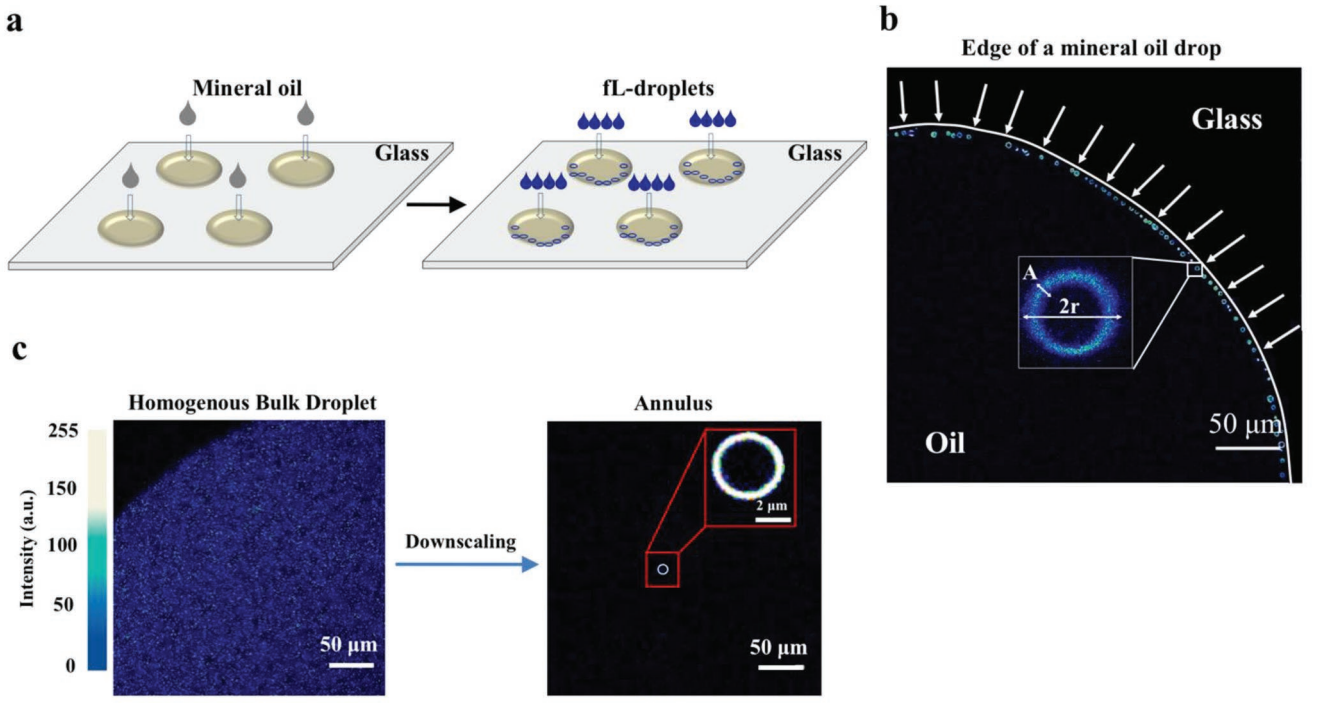

Figure 2. Autonomous assembly of annular crowded confined structures in fL-droplets. a) Injection of fL aqueous droplets (blue) produces micrometer droplets at the edge of the mineral oil drop arrayed on glass. b) Representative fluorescence images of a quasi-regular pattern of fL-droplets (containing 10×10^{-9} M Alexa647) at the edge of a nonfluorescent mineral oil drop. Each optical section of the fL-droplets shows a fluorescent annulus at its perimeter. The inset shows a single fL-droplet along with its diameter ($2r$) and the annulus thickness (A). The white curve marks the oil drop edge. c) The formation of a fluorescent annulus (40×10^{-9} M Atto655-labeled biotin) is observed by downscaling to fL-droplets and gives rise to an about 3.4-fold increase of molecular concentration with respect to HBDs.

2.2. Size-Induced Molecularly Crowded Confined Structures

About 5000 aqueous droplets at the fL-scale were injected in about 10 nL mineral oil drops arrayed with a spacing of 1 mm on a glass chip in a 4 × 2 format (see **Figure 2**a). Notably, fL-droplets are not stable in absence of F108, which has been observed to self-assemble at the water/oil interface[34] avoiding the above cited molecular diffusion to the oil phase.[42] Once injected in mineral oil drops, given the high surface tension gradient between water and oil, aqueous fL-droplets are subjected to Marangoni flows toward the border of the oil drop resulting in an almost-regular droplet pattern (see the Supporting Information for details).

We initially employed fL-droplets containing fluorescent dyes[43] (Alexa647 or Atto655-Biotin) to characterize the drops by confocal fluorescence microscopy. In Figure 2b, a representative confocal fluorescence microscopy image at a mineral oil drop edge, that is not fluorescent, is reported, where a pattern of micrometer-scale fL-droplets is observed. At the oil drop border, fL-droplets are regularly spaced with a distance of about 15 µm. By means of confocal microscopy it is possible to verify that printed droplets have a spherical shape. Here, optical sections of the droplets are acquired at about their equator, showing that the fluorescent signal is confined in annular regions at the droplet surface. The average droplet diameter ($2r$) and annuli thickness (A) are 4.0 ± 0.6 and 0.6 ± 0.1 µm, respectively (Figure 2b). In three dimensions, this results in confined spherical shells with a volume 3.4 ± 0.5 times smaller than the whole droplets. For simplicity, in the following, these structures will be referred as annuli, as their features observed by their optical sections. This geometrical confinement likely results in an up-concentration of molecules in the annuli that is specifically triggered by the droplet size reduction. Indeed, in the case of µL- and pL-scale drops, dye molecules homogeneously occupy the drop volume (hereafter homogeneous bulk droplets; HBDs). In fL-droplets, instead, we observe a remarkable molecular adsorption at the water/oil interface which might be the result of surface energy minimization (see Figures S4 and S5 in the Supporting Information for details). In Figure 2c, the fluorescent signal of the above sample in about 50 µL HBDs is presented in comparison with the downscaled fL-droplets with the annular structures.

By employing theoretical models describing the absorption of amphiphilic molecules at the interfaces of immiscible liquids,[44] it is possible to reveal that the molecular adsorption layer at the water/oil interface would result in a homogeneous concentration profile of molecules with a thickness (L_t) of about ≈500 nm (see the Supporting Information for details). Interestingly, this predicted L_t value is comparable to that experimentally observed in fL-droplets containing a model dye and the above amphiphilic systems. By considering that the molar ratio between the amphiphiles and the dye is about 1000:1, it is possible to infer that the annulus would consist mainly of F108–Tween-20 molecules enclosing the dye molecules.

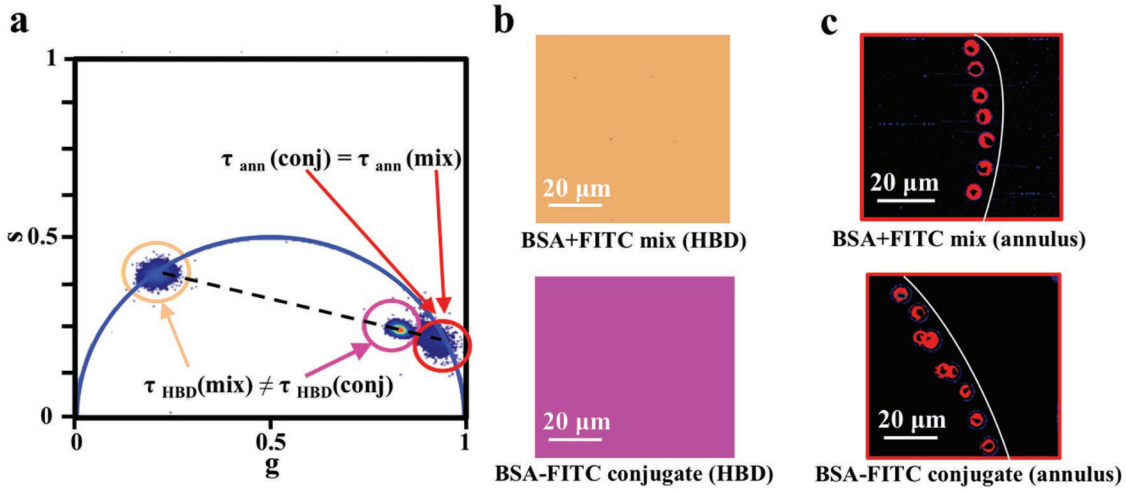

Figure 3. FLIM analysis of BSA–FITC systems. a) Phasor plot representing the fluorescence lifetime (τ) distributions in the annuli of fL-droplets for a BSA/FITC mixture (BSA 1.2×10^{-6} M, FITC 10×10^{-6} M; yellow cursor) and BSA–FITC conjugates (BSA–FITC 10×10^{-6} M; red cursor). b) Fluorescence lifetime selection maps for HBDs containing BSA/FITC mixture (orange) or BSA–FITC conjugates (magenta) with pixel signals showing lifetime distributions selected in the phasor plot by the circular cursors of the corresponding color. c) Fluorescence lifetime map in the annuli of fL-droplets colored in red for both the BSA/FITC mixture or the BSA–FITC conjugate. The lifetimes are highlighted in the image by the same color of the cursors in the phasor plot, in order to spatially separate pixels where different fluorescence lifetimes are measured. The white curve marks the oil drop edge.

2.3. FLIM Analysis of Molecular Probes in Molecularly Crowded Confined Structures

FLIM has been employed to investigate the physicochemical properties of fluorescent molecules in the annuli. Analysis of FLIM measurements was performed by the phasor approach,[45–47] which gives the graphical view of all the measured fluorescence decays at each pixel of the observed image. Separate clouds of pixels (selected with colored cursors) in the phasor plot stem for separate fluorescence lifetimes distributions measured at the image pixels. Long lifetimes are near the origin while short lifetimes are shifted on the circular line toward the bottom right (1 on the *x*-axis). The combinations of two single exponential components lie inside the semicircle and can be described as a linear combination of two monoexponential states.[32] It is possible to distinguish different lifetime distributions when they appear well separated in the phasor plot. In the following, we will report as τ the value of the average lifetime of fluorescence decay measured in pixels selected by the cursor.

The effect of annular confinement was first probed by measuring the τ distributions for model dyes (Figure S6, Supporting Information). The τ distributions of the environmental insensitive Alexa 647 dye[43] or the model viscosimeter CCVJ 9-(2-Carboxy-2-cyanovinyl) julolidine[48] do not significantly change within the annuli (Figure S6a,b, Supporting Information) with respect to the one measured in HBDs (see the Supporting Information). On the other hand, a significant τ reduction in annulus is observed for fluorescein isothiocyanate (FITC), a probe critically sensitive to the pH or the hydrogen-bond character of the environment[49] (τ_{ann} = 2 ns; τ_{HBD} = 4 ns; see Figure S6c in the Supporting Information). This reduction can be likely ascribed to the up-concentration of surfactants[44] and/or the water molecules depletion (crowding inducing excluded volume effects) within the annuli.[50]

The analysis of fluorescence lifetime distribution of FITC conjugated to the protein bovine serum albumin (BSA) is reported in **Figure 3** together with measurements on the mixture of the two molecules. The phasor plot of Figure 3a shows different lifetime distributions marked by three different cursors. The fluorescence lifetime selection maps for HBDs and for the annuli are reported in Figure 3b,c, respectively. The BSA/FITC mixtures (BSA 1.2×10^{-6} M; FITC 10×10^{-6} M) are shown in the upper panels whereas the BSA–FITC conjugates (BSA–FITC 10×10^{-6} M) samples are in the lower. The HBD fluorescence in Figure 3b is uniform and with the same lifetime distribution in the whole image both for the BSA–FITC conjugate (magenta cursor) and BSA/FITC mixtures (orange cursor). As expected, τ_{HBD}(mix) is centered at about 4 ns, that is close to the typical τ of free FITC.[50] On the other hand, the lifetime distribution of BSA–FITC conjugates – τ_{HBDs}(conj), is found inside the universal circle and it is significantly shorter than τ_{HBD}(mix), as expected.[51] Measurements in the annuli show critically different results, being the lifetime distributions for both the BSA–FITC conjugates – τ_{ann}(conj) and BSA/FITC mixtures – τ_{ann}(mix) superimposed at about 0.5 ns. These two indistinguishable τ distributions are selected by the red cursor in the phasor plot (see Figure 3a). Accordingly, the pixels in the selection maps are highlighted with the same color (Figure 3c). Interestingly, the τ distribution for the BSA–FITC conjugates in the annuli is significantly shorter than in HBDs. Note that the τ_{HBD}(conj) value lies on the straight dashed line (see Figure 3a) connecting the τ_{HBD}(mix) and the τ_{ann}(mix), as an indication that the fluorescence decay is more complex and can be characterized by a double exponential of these two lifetimes.[45] These results suggest that the environment experienced by FITC dye mixed in solution with BSA in the annuli is very similar to the one experienced by the same dye covalently bound to BSA. The observed effect can be rationalized by considering that the molecularly crowded confinement with excluded volume effects

can trigger nanometric scale intermolecular proximity.[52] Analogous results were found by employing Atto655-labeled biotin interacting with the tetravalent Streptavidin (Figure S7, Supporting Information). The different lifetime distributions of this model protein–ligand couple in the annuli with respect to HBDs may be ascribed to changes in the Streptavidin conformation and/or to larger quenching effects upon the formation of the Biotin–Streptavidin complex (see the Supporting Information for details).

2.4. CYP2E1 Enzymatic Process in the Molecularly Crowded Confined Structures

The data presented in the previous section have shown that molecular crowded confinement is generated in the fL-scale droplets. Here, we further investigated this environment by using biochemical reactions characterized by a higher level of complexity, as those typically occurring in cellular environments.

In particular, the assembly of complex metabolic processes in artificial microcompartments is fundamental for the construction of cell-like systems[1] and on this respect, it is important to optimize the spatial distribution[53] and the intermolecular distance[54] of enzymatic processes in subcellular scale compartments in presence of crowding and confinement. Accordingly, in the crowded cellular environments, metabolic reactions are assembled as spatially organized networks triggered by the interaction between different enzymes in response to chemical gradients of their enzymatic substrates, leading to emerging properties such as substrate channeling[54] and chemotaxis.[55] Among the enzymatic systems, the Cytochrome P450 2E1 (CYP2E1) is a cytochrome P450 phase I membrane protein whose expression in mitochondria is connected to type 2 diabetes, obesity, and ethanol intoxication.[56] Importantly, CYP2E1 in the mitochondrial matrix environment shows remarkable differences in the induction of oxidative stress with respect to the cytosol-exposed enzyme in the endoplasmic reticulum.[56]

In our experiments, we employ CYP2E1 as a model metabolic enzyme in artificial micrometric compartments in order to mimic a mitochondrial enzymatic process. This process involves the catalyzed hydroxylation of 7-(ethoxymethoxy)-2-oxo-2*H*-1-benzopyran-3-carbonitrile (EOMCC) to a fluorescent product, namely, 3-cyano-7-hydroxycoumarin (CHC) together with a regeneration system restoring the CYP2E1 activity through the NADPH produced by the reduction of $NADP^+$ with the glucose-6-phosphate dehydrogenase catalyzed oxidation of glucose-6-phosphate (see Figure S8 in the Supporting Information for details). Note that this behaves similarly to living systems where the CYP450 metabolic reactions are actively sustained by electron donors to produce active species of the enzymes.[56]

Sample droplets with the above described mixture in presence of different concentration of EOMCC (ranging from 5×10^{-6} to 40×10^{-6} M) have been injected into mineral oil drops. The fL-droplets were imaged as a function of time every 20 min up to 120 min. No significant fluorescence was detected at the beginning, but then the signal progressively grew. In stationary conditions, it is evident that the fluorescence signal, due to the formation of CHC, in line with previously analyzed systems, is confined at the edge of the drop and in shells with same spatial features. No further signal increase was observed after 120 min. Interestingly, **Figure 4**a shows that at the lowest EOMCC concentration (5×10^{-6} M), the fluorescence signal was discontinuously distributed at the annuli showing CHC-rich separated micrometer-sized regions (about 2 μm in size), hereafter defined as "spots." At increasing concentration of EOMCC, the spots in the confined regions grow in number and size until the full annulus is filled at about 20×10^{-6} M. At difference from measurements in HBD where the fluorescence signal is uniformly distributed, in the fL-droplets confined environment, a heterogeneity of the reaction product spatial distribution is observed.

In Figure 4b, the phasor plot of the CYP2E1 reaction ([EOMCC] = 20×10^{-6} M) in the annuli and in HBDs is reported in order to compare the τ distributions of CHC fluorescence. It is possible to observe a single distribution centered at about τ_{HBD} (CHC) = 3.6 ns (orange cursor), whereas the τ_{ann}(CHC) distribution is inside the phasor plot at shorter values, and can be considered as the combinations of two single exponential components.[32] The corresponding selection maps are reported in Figure 4c. Results can be interpreted by considering that CHC-fluorescence reflects differences in its environment. On this respect, hydroxycoumarins, such as CHC, have been observed to experience acid dissociation, leading to both the undissociated and dissociated phenolates with different fluorescence spectra depending on the environmental water content.[57] Accordingly, the above water exclusion effects within the annuli would lead to a reduction of τ by a significant presence of almost quenched undissociated phenolates which would coexist with the fluorescent dissociated form. The reaction product formation as a function of the EOMCC concentration is shown for HBDs and for the spots observed in the annuli at the EOMCC concentration of 20×10^{-6} M in Figure 4d,e, respectively. Fluorescence intensity growth in Figure 4d qualitatively takes in account for CHC formation as a function of EOMCC concentration and indicates that the reaction profile in HBDs is in good agreement with experiments in larger bulk volumes.[58] As shown in Figure 4f where the average fluorescence measured in the spots is reported as function of the EOMCC concentration, an analogous behavior is observed indicating that such a complex reaction is still occurring in the annuli of fL-droplets.

Notably, heterogeneous distribution of products in enzymatic reactions, highlighted in these experiments, has previously been observed in other enzymatic systems. Recently, Zhao et al. observed spots at similar sizes in microfluidic-based platforms, due to glycolysis cascade enzyme chemotactic assemblies induced by their specific substrates in crowded conditions.[59] In our case, the localization of CHC in spots can be the result of crowding in environments with limited water content, i.e., a condition where protein–protein interactions have been observed triggering phase separation in intracellular environments.[11] On the other side, at high EOMCC concentrations, the more uniform CHC signal from the annuli would be consistent with the lateral growth of the CHC-rich zones as well as with a lower probability to generate chemotactic-driven enzymatic assembly.[59] The CYP2E1-catalyzed reaction in highly concentrated regions (annuli and/or spots) may be interestingly related to its different reactivity in mitochondria and in endoplasmic reticula.[56] Indeed, the different reactivity takes account

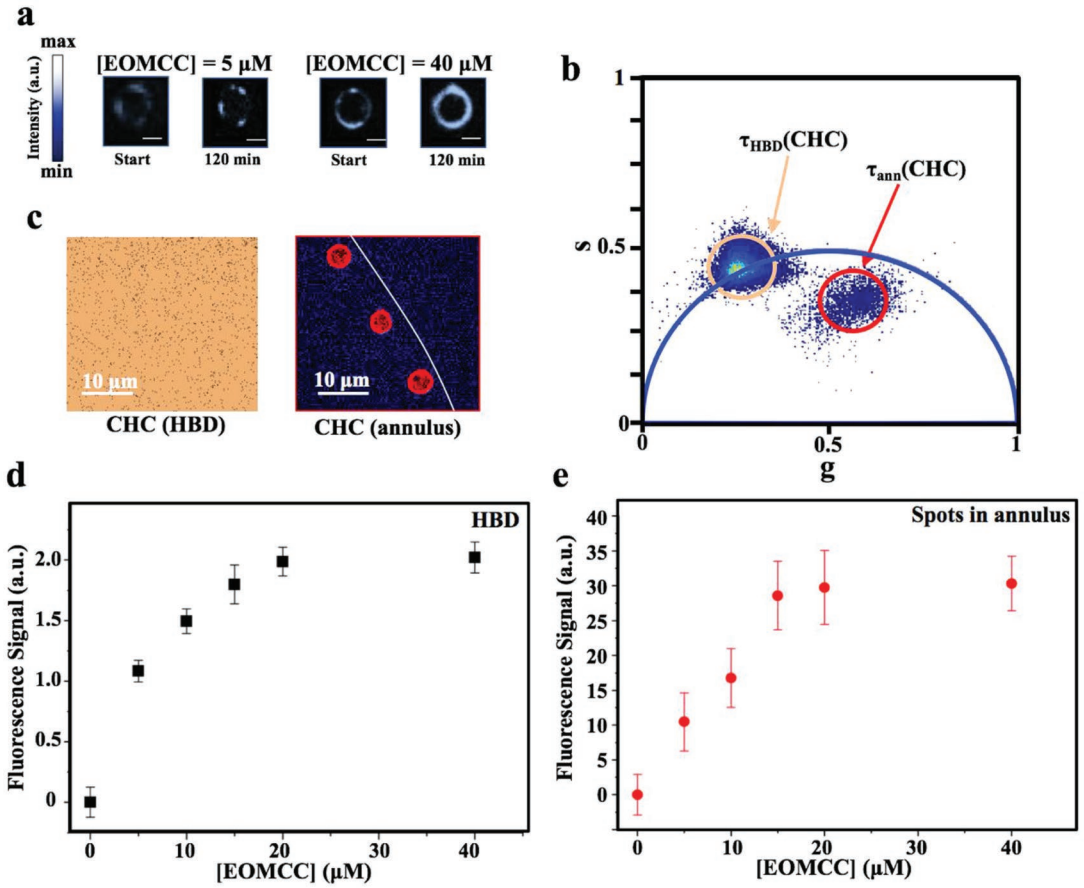

Figure 4. Model mitochondrial reaction in the annuli giving heterogeneous distribution of reaction products. a) Heterogeneous distribution of CHC-rich spots at the annulus for two selected EOMCC concentrations (5×10^{-6} and 40×10^{-6} M) at the start of the reaction and after 120 min. Scale bar is equal to 2 µm. b) The CYP2E1-catalyzed reaction shows a single exponential fluorescence lifetime distribution in HBDs (orange cursor) and a more complex lifetime distribution within the annuli (red cursor) which can be ascribed to the presence of the two CHC species (undissociated and dissociated) as a result of water molecules depletion in the annulus. c) Corresponding fluorescence lifetime map for the samples in (b) (orange color for HBDs; red for annuli). The white curve marks the oil drop edge. CHC fluorescence in HBDs (black squares in panel (d)) and in the spot structures observed in the annuli (red circles in panel (e)) as a function of the EOMCC concentration. For both (d) and (e), $n = 10$. Error bars represent standard deviation. Note that in the case of annuli, the reported [EOMCC] values stand for the printed concentration of EOMCC in the fL-droplet.

not only of the enzyme-substrate affinity (in mitochondria, CYP2E1 has been observed with a more unfolded conformation and a markedly reduced α-helical contents compared with the cytosolic CYPs[56]) but more specifically of the localization of the whole enzymatic processes involving the enzyme regeneration system and/or the CYP2E1-mediated production of reactive oxygen species finally producing more toxic effects in mitochondria than in the cytosol.[56]

2.5. DNA Hairpins in the Molecularly Crowded Confined Structures

DNA hairpins are reactive DNA structures formed by intrastrand base pairing of a sequence containing two self-complementary portions.[60] They are used here as model systems to evaluate the folding/unfolding behavior of biomolecules in artificial subcellular-like environment.[61,62] **Figure 5**a shows the DNA hairpin with a fluorophore (Alexa555) at 5′ and a black hole quencher (BHQ-2) at 3′ allowing for Förster resonance energy transfer (FRET). Hybridization of the DNA hairpin with a DNA sequence complementary to the loop portion (input) converts the hairpin into a double-helical segment with Alexa 555 away from the quencher, thus allowing for fluorescence emission (ON-state). Figure 5b reports the phasor plot with the τ distributions of Alexa 555 bound to the DNA hairpin (10×10^{-9} M) in the absence (OFF-state) and in the presence (ON-state) of the DNA input (500×10^{-9} M) for both HBDs and the annuli in fL-droplets. Molecules in the annuli are about 3.4-fold more concentrated than in HBDs. Control experiments carried out in HBDs at about 3.4-fold higher concentration, i.e., a condition where all molecules and buffer concentrations are similar to that in the annuli, exclude up-concentration effects since no differences in the τ distribution are observed. The Alexa 555 τ in the OFF-state in HBDs is not measurable, while in the annuli (magenta cursor) τ_{ann}(OFF) is about 0.2 ns. In the same environment, the DNA ON-state shows in the annuli (red cursors) τ_{ann}(ON) = 0.9 ns to be compared to that in HBDs (orange cursor) τ_{HBD}(ON) = 0.6 ns. The corresponding selection maps for all the analyzed samples are reported in Figure 5c.

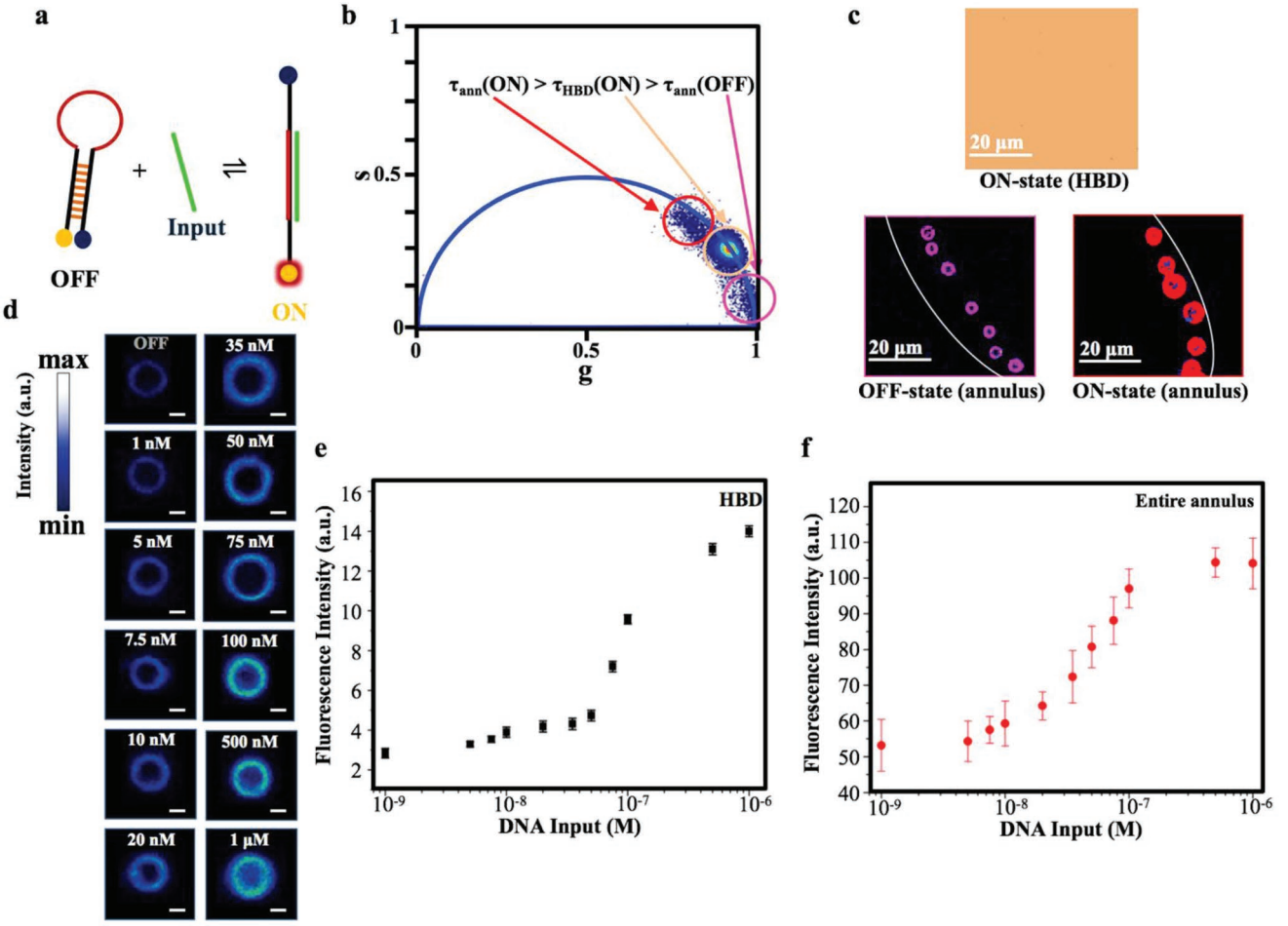

Figure 5. DNA hairpin reactivity in confined annuli. a) DNA hairpin switching from the OFF-state to the double helix ON-state by the action of a DNA target input. b) τ distributions of DNA in ON-state in HBDs (orange cursor) and in the annuli of fL-droplets (red cursor). DNA in OFF-state shows a detectable τ (magenta cursor) only when confined in the annuli. c) Fluorescence lifetime maps uniformly colored in orange in the case of the DNA in ON-state in HBDs. All the fluorescence lifetime pixels in the annuli are colored in red for DNA in ON-state and in magenta for DNA in OFF-state. The white curve marks the oil drop edge. d) Fluorescence images of annuli containing DNA hairpin at 10×10^{-9} M in presence of increasing concentration of the DNA input. Scale bar is equal to 2 µm. Fluorescence intensity in HBDs (black squares in panel (e)) and in the annuli (red circles in panel (f)) as a function of the number of DNA input concentration. For both (e) and (f), $n = 5$. Error bars represent standard deviation. Note that in the case of annuli, the concentration values stand for the printed concentration of DNA input in the fL-droplet.

In order to monitor the DNA hairpin OFF to ON switch, droplets containing mixtures of DNA hairpin and DNA input were printed and the fluorescence signal was collected after 30 min. Representative images of fL-droplets containing Alexa 555–DNA hairpin showing a fluorescence growth with the printed concentration of the DNA input (from 1×10^{-9} to 1×10^{-6} M) are reported in Figure 5d, the fluorescence signal being homogeneously localized in the annuli with thickness of 580 ± 70 nm. The fluorescence intensity of DNA hairpins as a function of the DNA input amount is reported for HBDs and for the annuli in Figure 5e,f, respectively. As expected, DNA hairpin in HBDs shows an insignificant fluorescence signal due to the Alexa555 quenching by BHQ-2 (the measured fluorescence intensities are comparable to the background noise). On the other hand, as reported in Figure 5d, DNA hairpin in the annuli shows a nonzero fluorescence in absence of input. DNA hairpin signal is completely quenched in 3.4-fold up-concentrated HBDs, so that we can exclude that this effect is due to up-concentration and it might be more likely ascribed to the interaction between the molecular systems with the confined environment and/or to a slight difference in the initial DNA hairpin conformation.[62] Notwithstanding this difference, the fluorescence signal as a function of the input concentration shows in the annuli of fL-droplets again a sigmoidal shape indicating an efficient ON–OFF switching.

3. Conclusion

This paper reports on the development of a new versatile lab-on-chip platform to prepare and characterize life-inspired subcellular compartment very well defined in dimension, composition, and concentration by advanced printing and fluorescence techniques.

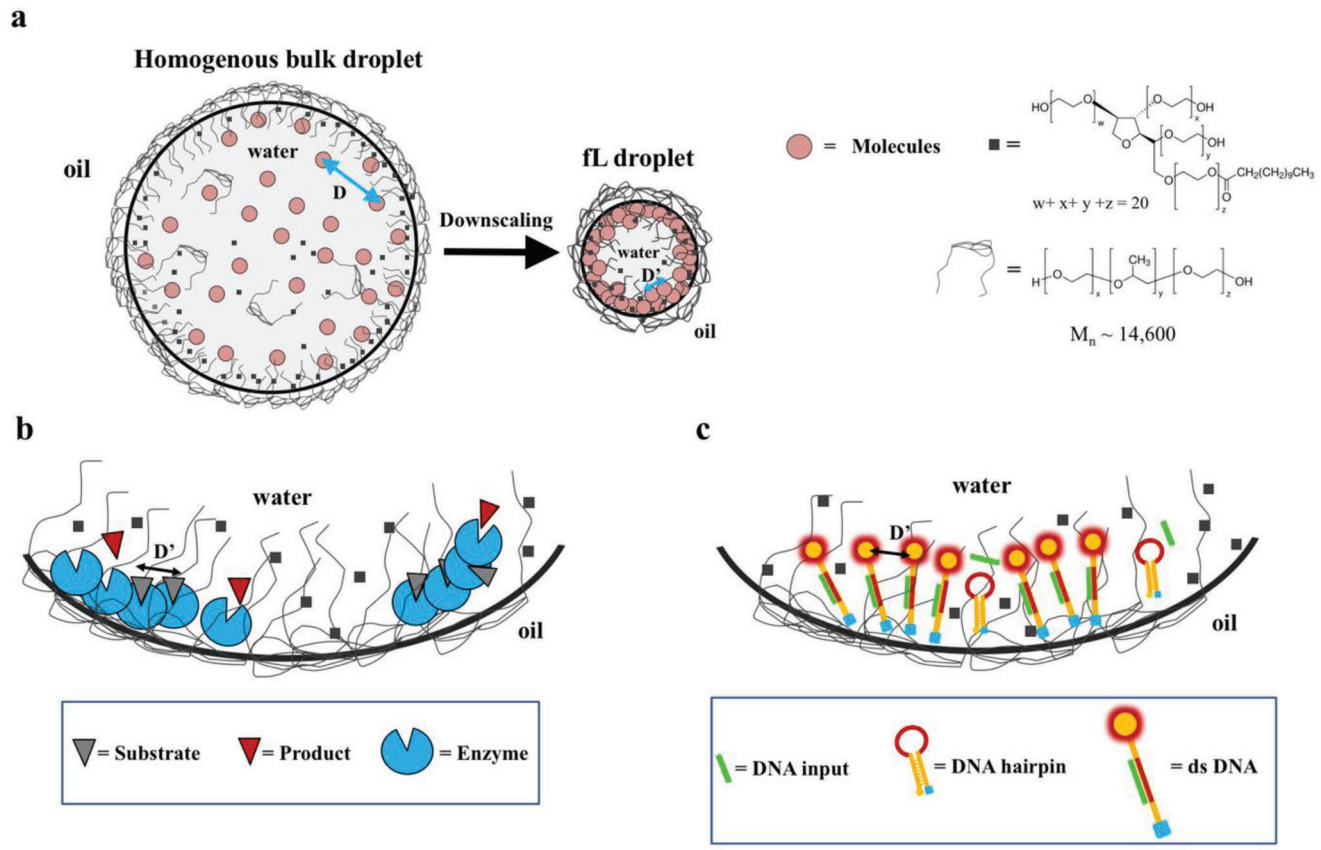

Figure 6. Schematic representations of molecular crowded confinement through amphiphilic layers with embedded molecular systems by downscaling the size of stabilized water droplets: a) the transition from HBDs to fL-droplets triggers interfacial molecular assemblies with closer intermolecular distances (*D'*); b,c) restricted regions of fL-droplet surfaces showing discontinuous spots of enzymatic reaction products and DNA hairpins still responsive to molecular triggers under conformational changes, respectively. Note that, for the sake of simplicity, the figures only show the adsorption of a single molecular layer at the water/oil interface, whereas in real systems, it would consist of an ≈500 nm thick layer.

From the fundamental point of view, we demonstrated the onset of different new features by precisely downscaling at the fL-volume or few µm size regime, i.e., the same dimension of subcellular complex compartments. In contrast to larger droplets, this size regime results in the spontaneous confinement of hundreds of nanometers thin shell molecular structures at crowded liquid/liquid interfaces stabilized by amphiphilic molecules. These structures enclose crowded assemblies of selected molecular or biomolecular systems (**Figure 6**a). In effect, nature employs analogues phase separation mechanisms to include precious sets of functional biomolecules within membrane bound organelles (e.g., mitochondria, nuclei) and membrane-less systems (P-bodies, Cajal bodies, etc.).[11] Thus, in addition to the intermolecular interaction, for these systems, their complex function within the cellular economy is likely related to their size regime allowing for both enough volume space and a peculiar surface/volume ratio driving phase separation phenomena.[8] Accordingly, other subcellular compartments typically experiencing more simple functions (e.g., transport) may take smaller (nanoscopic) sizes not showing the above structural features.[8]

Emerging properties of the here studied confined systems include up-concentration, molecular proximity, and decreased water content. Our studies reveal that the crowded confinement triggers an unprecedented heterogeneity in the spatial organization of reaction products generated by mitochondrial enzymatic reactions (Figure 6b). This highlights the importance of the spatial distribution and the intermolecular distances in fL-scale subcellular compartments. Notwithstanding confinement might induce subtle conformational changes to biomolecules (i.e., proteins and DNA hairpins), these maintaining their functional features and responsivity to molecular triggers (Figure 6c).

We believe that the above findings would result in different technological and fundamental perspectives. At first, the above lab-on-chip platform provides an important tool for discovering the roles of confinement and crowding in the functionality of cellular and subcellular compartments. Also, this platform may provide an alternative approach to prepare programmed protocells as well as very well defined artificial smart organelles to be incorporated in living cells to complement or affect the cellular processes.[3] Finally, it will be possible to study the correlation between the structure, the properties, and the function of molecular assemblies in very well defined subcellular compartments under very well controlled physiological and pathologic conditions.[11]

4. Experimental Section

Chemicals and Solution Preparation: Mineral oil (light oil-neat, Sigma-Aldrich), 1*H*,1*H*,2*H*,2*H*-perfluorooctyltriethoxysilane (Sigma-Aldrich), Tween-20 (polyoxyethylene (20) sorbitan monolaurate, Sigma-Aldrich), Poly(ethylene glycol)-block-poly(propylene glycol)-block-poly(ethylene glycol) – F108, Alexa 647 (Alexa Fluor 647 carboxylic acid, succinimidyl ester, ThermoFisher Scientific), fluorescein sodium (FITC, suitable for fluorescence, Sigma-Aldrich), bovine serum albumin (Sigma-Aldrich, lyophilized powder, ≥96.0%), albumin–fluorescein isothiocyanate conjugate bovine (BSA–FITC, Sigma-Aldrich), 9-(2-Carboxy-2-cyanovinyl) julolidine BioReagent (CCVJ) (Sigma-Aldrich suitable for fluorescence, ≥97.0% HPLC), Atto655 biotin (Bio-Reagent, suitable for fluorescence, Sigma-Aldrich), and Streptavidin from *Streptomyces avidinii* (lyophilized from 10×10^{-3} M potassium phosphate, Sigma-Aldrich) were purchased and used as received. With the exception of DNA hairpin and CYP2E1 assay, a buffer solution containing 100×10^{-3} M phosphate (pH 7.4), 0.05% v/v Tween-20, and 0.03% w/v F108 was employed for all the experiments. In the case of DNA hairpin solutions, NaCl at the final concentration of 50×10^{-3} M was added. All aqueous solutions were prepared in ultrapure Millipore water (Direct Q-UV filtration system, 18.2 MΩ cm). The pH was controlled by a pH meter (pH 700, Eutech Instruments).

DNA Sequences: All oligonucleotides were synthesized, labeled, and purified (HPLC and reverse phase) by IBA GmBH (Göttingen, Germany). Oligonucleotides were dissolved in PBS buffer at a concentration of 100×10^{-6} M, confirmed using Tecan Infinite M200pro (Männedorf, Switzerland) through NanoQuant Plate.

The sequences used for the experiments were:

#1 *DNA hairpin*: t(Alexa555) gagcgGTATAGCCTAATTCGcgctct (BHQ-2) ctgtcactttctgag -3′.

#2 *DNA input*: 5′-DNPttttttttttttttttCGAATTAGGCTATAC-3′

Strand #1 was terminally modified with Alexa555 and internally with black hole quencher 2.

CYP2E1 Assays: CYP2E1 assay kit (Life Technologies) contained: Vivid CYP2E1 substrate (EOMCC 7-(ethoxymethoxy)-2-oxo-2*H*-1-benzopyran-3-carbonitrile 0.1 mg), $NADP^+$ (10×10^{-3} M in 100×10^{-3} M potassium phosphate buffer pH 8.0), Vivid Regeneration System (333×10^{-3} M glucose-6-phosphate and 30 U mL^{-1} glucose-6-phosphate dehydrogenase in 100×10^{-3} M potassium phosphate buffer pH 8.0), and microsomes from baculovirus-infected cells coexpressing CYP2E1, NADPH-cytochrome P450 reductase, and cytochromeb5 (CYP2E1 Baculosomes 0.5 nmol in 100×10^{-3} M potassium phosphate buffer pH 7.4).

Inkjet Printing fL-Scale Aqueous Solutions on Glass Surfaces: Droplets were dispensed on glass substrates by a Dimatix Materials Printer (DMP-2800, Fuji Film) at 40% relative humidity. This instrument was equipped with piezodriven inkjet print cartridges, each with 16 nozzles 254 μm spaced and 21.5 μm (for 10 pL cartridge) or 10.5 μm (for 1 pL cartridge) in diameter. Mineral oil droplets were dispensed by using conventional waveform at 5 kHz and 10 pL cartridges at temperatures of 33 °C and at voltages of 28–30 V. An ensemble of 1000 oil droplets (droplet-to-droplet pitch of 5 μm) formed a single droplet of about 10 nL by coalescence. Mineral oil microarrays were fabricated in a 4×2 format of 10 nL drops with a spacing of 1 mm. About $5{\cdot}10^3$ fL-scale aqueous droplets with a drop-to-drop pitch of 40 μm were injected in the oil drops by using the designed waveform at 1.2 KHz and 1 pL cartridges at room temperature and at voltages of 12–14 V. Water-in-oil droplet microarrays were fabricated on coverslip glasses (Corning 24×50 mm, 0.13–0.16 thick), functionalized following reported protocols.[31]

Confocal Microscopy and FLIM Analysis: Confocal images of fL-droplets were acquired in one channel with an Olympus FluoView1200 confocal laser scanning microscope (Olympus) using a 60×1.35 NA objective. 515 nm laser was used to excite the Alexa 555 dye of DNA hairpin. The bandwidth of the emission filter used for the red emission channel was 550–650 nm. Data were collected in the photon-counting mode. The scan area was 512×512 pixels, the pixel size was set at 0.05 μm, and the scan speed was 4 μs per pixel. Images were analyzed by Image J software (1.46r version). For FLIM analysis, 256×256 pixels image stacks were sequentially acquired using a Leica TCS SP5 confocal scanning microscope with a 63×1.4 NA objective (Leica Microsystems, Germany), scan frequency was 400 kHz. For the CCVJ, 2-photon excitation was set at 830 nm and the detection range at 450–650 nm, while for the CYP2E1 catalyzed reaction the 2-photon excitation was set at 810 nm, the detection range at 440–520 nm. Leica "white laser" was used for the excitation of FITC, Alexa 647, Atto655-BTN, and DNA hairpin, and was set at 488, 647, 655, and 515 nm, respectively. Fluorescence decay was initially evaluated with the SymPhotime Analysis software; FLIM images were analyzed using the SimFCS 3.0 program (Laboratory for Fluorescence Dynamics, University of California, Irvine, CA) to calculate the fluorescence lifetime with the phasor method.[45] Droplets confocal images for CYP2E1 assays were acquired with the Leica TCS SP5 confocal scanning microscope; fluorescence intensity values of bulk solutions and fL-droplets were obtained by Image J software (1.46r version).

Statistical Analysis: All the data concerning the fL-scale droplets formation dynamics (i.e., droplet radius and thread length, pinch-off time, droplet speed) were presented as mean ± standard deviation and were derived from five different stroboscopic images. All the fluorescence intensity data were presented as mean ± standard deviation and were obtained from confocal microscopy images of at least five different droplets. In the case of the CYP2E1 enzymatic assay, the fluorescence intensity data were obtained from spots in the annular regions and subtracted from the intensity value in the absence of the enzymatic substrate (EOMCC). In the case of DNA hairpin, the reported fluorescence data were selected from the whole annular regions and were unmodified. FLIM on annular regions of fL-droplets were carried out by replicating the analysis on six different maps (each containing typically six droplets) to obtain a signal/noise ratio comparable to that of HBDs.

Supporting Information

Supporting Information is available from the Wiley Online Library or from the author.

Acknowledgements

G.A. and F.C. contributed equally to this work. This work was funded by the MiUR (PRIN 2013 program, PRIN 2012CTAYSY_003, pursuing new horizons for cancer therapy through the integration of innovative high-throughput drug-screening and rational drug-discovery). Aten Center, Università degli Studi di Palermo, is acknowledged for service.

Conflict of Interest

The authors declare no conflict of interest.

Keywords

biomolecular confinement, DNA hairpins, inkjet printing, life-like compartments, molecular crowding

Received: February 20, 2019
Revised: April 3, 2019
Published online: May 3, 2019

[1] B. C. Buddingh', J. C. M. Van Hest, *Acc. Chem. Res.* **2017**, *50*, 769.
[2] B. Städler, A. D. Price, A. N. Zelikin, *Adv. Funct. Mater.* **2011**, *21*, 14.
[3] T. Einfalt, D. Witzigmann, C. Edlinger, S. Sieber, R. Goers, A. Najer, M. Spulber, O. Onaca-Fischer, J. Huwyler, C. G. Palivan, *Nat. Commun.* **2018**, *9*, 1.

[4] E. Altamura, F. Milano, R. R. Tangorra, M. Trotta, O. H. Omar, P. Stano, F. Mavelli, *Proc. Natl. Acad. Sci. USA* **2017**, *114*, 3837.
[5] V. Kapoor, D. Wendell, *Nano Lett.* **2013**, *13*, 2189.
[6] K. Y. Lee, S. J. Park, K. A. Lee, S. H. Kim, H. Kim, Y. Meroz, L. Mahadevan, K. H. Jung, T. K. Ahn, K. K. Parker, K. Shin, *Nat. Biotechnol.* **2018**, *36*, 530.
[7] B. V. V. S. P. Kumar, A. J. Patil, S. Mann, *Nat. Chem.* **2018**, *10*, 1154.
[8] S. F. Banani, H. O. Lee, A. A. Hyman, M. K. Rosen, *Nat. Rev. Mol. Cell Biol.* **2017**, *18*, 285.
[9] B. Zhang, Y. H. Koh, R. B. Beckstead, V. Budnik, B. Ganetzky, H. J. Bellen, *Neuron* **1998**, *21*, 1465.
[10] M. Gao, C. Held, S. Patra, L. Arns, G. Sadowski, R. Winter, *ChemPhysChem* **2017**, *18*, 2951.
[11] Y. Shin, C. P. Brangwynne, *Science* **2017**, *357*, eaaf4382.
[12] P. Montero Llopis, A. F. Jackson, O. Sliusarenko, I. Surovtsev, J. Heinritz, T. Emonet, C. Jacobs-Wagner, *Nature* **2010**, *466*, 77.
[13] H. D. Ou, S. Phan, T. J. Deerinck, A. Thor, M. H. Ellisman, C. C. O'Shea, *Science* **2017**, *357*, eaag0025.
[14] A. Aizer, A. Kalo, P. Kafri, A. Shraga, R. Ben-yishay, A. Jacob, N. Kinor, *J. Cell Sci.* **2014**, *127*, 4443.
[15] M. M. K. Hansen, L. H. H. Meijer, E. Spruijt, R. J. M. Maas, M. V. Rosquelles, J. Groen, H. A. Heus, W. T. S. Huck, *Nat. Nanotechnol.* **2016**, *11*, 191.
[16] H. Zhao, S. Sen, T. Udayabhaskararao, M. Sawczyk, K. Kučanda, D. Manna, P. K. Kundu, J.-W. Lee, P. Král, R. Klajn, *Nat. Nanotechnol.* **2016**, *11*, 82.
[17] C. A. Strulson, R. C. Molden, C. D. Keating, P. C. Bevilacqua, *Nat. Chem.* **2012**, *4*, 941.
[18] M. Miyazaki, M. Chiba, H. Eguchi, T. Ohki, S. Ishiwata, *Nat. Cell Biol.* **2015**, *17*, 480.
[19] A. Gupta, H. B. Eral, T. A. Hatton, P. S. Doyle, *Soft Matter* **2016**, *12*, 2826.
[20] K. Göpfrich, I. Platzman, J. P. Spatz, *Trends Biotechnol.* **2018**, *36*, 938.
[21] Y. Liu, S. Y. Jung, C. P. Collier, *Anal. Chem.* **2009**, *81*, 4922.
[22] X. L. Guo, Y. Wei, Q. Lou, Y. Zhu, Q. Fang, *Anal. Chem.* **2018**, *90*, 5810.
[23] T. Sekitani, Y. Noguchi, U. Zschieschang, H. Klauk, T. Someya, *Proc. Natl. Acad. Sci. USA* **2008**, *105*, 4976.
[24] Y. Zhang, B. Zhu, Y. Liu, G. Wittstock, *Nat. Commun.* **2016**, *7*, 12424.
[25] Y. Zhang, D. Li, Y. Liu, G. Wittstock, *Small* **2018**, *14*, 1801212.
[26] Y. Zhang, D. Li, Y. Liu, G. Wittstock, *Small* **2018**, *14*, 1802583.
[27] Y. Zhang, B. Zhu, G. Wittstock, D. Li, Y. Liu, *Sens. Actuators, B* **2018**, *255*, 2011.
[28] G. Arrabito, V. Errico, A. De Ninno, F. Cavaleri, V. Ferrara, B. Pignataro, F. Caselli, *Langmuir* **2019**, *35*, 4936.
[29] G. Arrabito, B. Pignataro, *Anal. Chem.* **2012**, *84*, 5450.
[30] G. Arrabito, C. Musumeci, V. Aiello, S. Libertino, G. Compagnini, B. Pignataro, *Langmuir* **2009**, *25*, 6312.
[31] G. Arrabito, F. Cavaleri, V. Montalbano, V. Vetri, M. Leone, B. Pignataro, *Lab Chip* **2016**, *16*, 4666.
[32] J. Eggers, *Phys. Rev. Lett.* **1993**, *71*, 3458.
[33] T. W. G. van der Heijden, A. A. Darhuber, P. van der Schoot, *Langmuir* **2018**, *34*, 12471.
[34] A. Caciagli, M. Zupkauskas, A. Levin, T. P. J. Knowles, C. Mugemana, N. Bruns, T. O'Neill, W. J. Frith, E. Eiser, *Langmuir* **2018**, *34*, 10073.
[35] B. Derby, *Annu. Rev. Mater. Res.* **2010**, *40*, 395.
[36] J. S. Nambam, J. Philip, *J. Phys. Chem. B* **2012**, *116*, 1499.
[37] K. Szymczyk, M. Szaniawska, A. Taraba, *Colloids Interfaces* **2018**, *2*, 34.
[38] K. Patel, P. Bahadur, C. Guo, J. H. Ma, H. Z. Liu, Y. Yamashita, A. Khanal, K. Nakashima, *Eur. Polym. J.* **2007**, *43*, 1699.
[39] M. R. R. Niño, J. M. R. Patino, *J. Am. Oil Chem. Soc.* **1998**, *75*, 1241.
[40] B. He, S. Yang, Z. Qin, B. Wen, C. Zhang, *Sci. Rep.* **2017**, *7*, 11841.
[41] G. M. Nishioka, A. A. Markey, C. K. Holloway, *J. Am. Chem. Soc.* **2004**, *126*, 16320.
[42] P. Gruner, B. Riechers, B. Semin, J. Lim, A. Johnston, K. Short, J.-C. Baret, *Nat. Commun.* **2016**, *7*, 10392.
[43] N. Panchuk-Voloshina, R. P. Haugland, J. Bishop-Stewart, M. K. Bhalgat, P. J. Millard, F. Mao, W.-Y. Leung, R. P. Haugland, *J. Histochem. Cytochem.* **1999**, *47*, 1179.
[44] M. Staszak, *J. Surfactants Deterg.* **2016**, *19*, 297.
[45] M. A. Digman, V. R. Caiolfa, M. Zamai, E. Gratton, *Biophys. J.* **2008**, *94*, L14.
[46] C. Stringari, A. Cinquin, O. Cinquin, M. A. Digman, P. J. Donovan, E. Gratton, *Proc. Natl. Acad. Sci. USA* **2011**, *108*, 13582.
[47] C. Sartorio, V. Campisciano, C. Chiappara, S. Cataldo, M. Scopelliti, M. Gruttadauria, F. Giacalone, B. Pignataro, *J. Mater. Chem. A* **2018**, *6*, 3884.
[48] J. A. Levitt, P.-H. Chung, M. K. Kuimova, G. Yahioglu, Y. Wang, J. Qu, K. Suhling, *ChemPhysChem* **2011**, *12*, 662.
[49] N. Klonis, A. H. A. Clayton, E. W. Voss, W. H. Sawyer, *Photochem. Photobiol.* **1998**, *67*, 500.
[50] M. M. Martin, *Chem. Phys. Lett.* **1975**, *35*, 105.
[51] G. Hungerford, J. Benesch, J. F. Mano, R. L. Reis, *Photochem. Photobiol. Sci.* **2007**, *6*, 152.
[52] A. P. Minton, *J. Biol. Chem.* **2001**, *276*, 10577.
[53] C. M. Agapakis, P. M. Boyle, P. A. Silver, *Nat. Chem. Biol.* **2012**, *8*, 527.
[54] I. Wheeldon, S. D. Minteer, S. Banta, S. C. Barton, P. Atanassov, M. Sigman, *Nat. Chem.* **2016**, *8*, 299.
[55] J. Agudo-Canalejo, P. Illien, R. Golestanian, *Nano Lett.* **2018**, *18*, 2711.
[56] S. Bansal, C. P. Liu, N. B. V. Sepuri, H. K. Anandatheerthavarada, V. Selvaraj, J. Hoek, G. L. Milne, F. P. Guengerich, N. G. Avadhani, *J. Biol. Chem.* **2010**, *285*, 24609.
[57] M. Takakusa, *J. Phys. Chem.* **1979**, *83*, 810.
[58] B. D. Marks, R. W. Smith, H. A. Braun, T. A. Goossens, M. Christenson, M. S. Ozers, C. S. Lebakken, O. V Trubetskoy, *Assay Drug Dev. Technol.* **2002**, *1*, 73.
[59] X. Zhao, H. Palacci, V. Yadav, M. M. Spiering, M. K. Gilson, P. J. Butler, H. Hess, S. J. Benkovic, A. Sen, *Nat. Chem.* **2018**, *10*, 311.
[60] L. Wang, G. Arrabito, *Analyst* **2015**, *140*, 5821.
[61] L. E. Baltierra-jasso, M. J. Morten, L. La, S. D. Quinn, S. W. Magennis, *J. Am. Chem. Soc.* **2015**, *137*, 16020.
[62] S. Patra, C. Anders, N. Erwin, R. Winter, *Angew. Chem., Int. Ed.* **2017**, *56*, 5045.

